Collaborative framework for PIV uncertainty quantification: comparative assessment of methods

Andrea Sciacchitano[1,*], Douglas R. Neal[2], Barton L. Smith[3], Scott O. Warner[3], Pavlos P. Vlachos[4], Bernhard Wieneke[5], Fulvio Scarano[1]

1: Department of Aerospace Engineering, Delft University of Technology, Delft, The Netherlands
2: LaVision Inc, Ypsilanti, MI, USA
3: Department of Mechanical and Aerospace Engineering, Utah State University, Logan, UT, USA
4: Department of Mechanical Engineering, Purdue University, Lafayette, IN, USA
5: LaVision GmbH, Göttingen, Germany

* correspondent author: a.sciacchitano@tudelft.nl

Abstract The topic of *a-posteriori* uncertainty quantification of Particle Image Velocimetry (PIV) data is recognized as crucial step to obtain accurate estimates of the uncertainty for a specific experiment. This is particularly relevant in the fluid dynamics community, especially when PIV measurements are employed for CFD data validation. In spite of the relevance of the subject, the first uncertainty quantification methods have been developed only in the last two years. The present work describes a comparative assessment of four approaches proposed in literature: the *uncertainty surface* method (Timmins *et al*, 2012), the *particle disparity* approach (Sciacchitano *et al*, 2013; called *image-matching* approach in this reference), the *peak ratio* approach (Charonko and Vlachos, 2013) and the *correlation statistics* method (Wieneke and Prevost, 2014). The analysis makes use of a data base produced during a dedicated experiment where the instantaneous velocity field is known with high accuracy by means of an independent and more accurate measurement system. Strengths and limitations of the four uncertainty quantification approaches observed within the different flow regimes and imaging conditions are discussed.

1 Introduction

Particle image velocimetry (PIV) is nowadays recognized as a standard flow diagnostic tool for fluid dynamics research, with a wide range of applications from supersonic flows to microfluidics. As in any other technique, the measurement errors in PIV are defined as the difference between measured value and true value and are typically classified into systematic (or bias) and random errors (Coleman and Steele, 2009). The systematic errors do not change during the measurement and are usually ascribed to calibration errors or to the inadequacy of the interrogation algorithm, typically based on the statistical operator of cross-correlation, in the evaluation of the PIV recordings. Examples of systematic errors are those occurring when the particle image diameter is of the order of one pixel (*peak locking*, Westerweel, 1997): in this case, the peak fitting algorithm is unable to correctly evaluate the average particle image displacement with sub-pixel accuracy. Instead, the random errors change from case to case, depending on several factors, such as background noise or out-of-focus in the recordings, out-of-plane particle motion and inhomogeneous seeding density.
The evaluation of PIV measurement errors has been investigated thoroughly in the last two decades either via theoretical modelling of the processing algorithm (Westerweel, 1997) or more frequently by Monte Carlo simulations (Scarano and Riethmuller, 2000; Lecordier *et al*, 2001, among others). In the latter approach, computer generated recordings with particle images are considered where the tracer particles move according to a known velocity field. As a result, the evaluation of the measurement error is straightforward and typically yields a figure of 0.03 to 0.1 pixels as measurement precision depending on several factors, including the cross-correlation algorithm adopted for the analysis (Raffel *et al*, 2007). It is acknowledge that Monte Carlo simulations underestimate the errors occurring in PIV experiments because too idealized conditions are usually considered (Stanislas *et al*, 2005).
Instead, in experiments the measurement error is typically unknown. Uncertainty quantification (UQ) estimates a possible value for the error and provides the experimenter a rational way of evaluating the

significance of the scatter on repeated trials (Moffat, 1988). This topic is crucial especially when PIV measurements are used to validate computational fluid dynamics (CFD) results. In spite of the relevance of the subject, to date no standard approach for the *a-posteriori* uncertainty quantification of PIV data exists. Only in the last two years, the first uncertainty quantification methods have been proposed that estimate the uncertainty bands of each measured vector based on considerations on the error sources, the correlation function or the matching between paired particle images.
The current work employs a dedicated experimental data base presented in another article within the same conference (Neal *et al*, 2014). The comparative assessment of different uncertainty quantification methods is based on the specific knowledge of the actual velocity by means of simultaneous measurements with independent and more accurate systems. The final aim of the work is investigating strength and limitations of current approaches in flow regimes and imaging conditions representative of typical wind tunnel experiments.

1.1 Background - description of the uncertainty quantification methods

Four approaches for the *a-posteriori* quantification of the instantaneous local uncertainty are assessed. Those approaches make use of information on the PIV recordings or the cross-correlation function to determine the uncertainty of the PIV measurement; the input and output quantities of those methods are summarized in table 1. Since the four methods return different output, for a fair comparison only the uncertainty of the *x*-velocity component is considered in the following. For the surface method, such quantity is evaluated as the maximum of lower and upper uncertainty bounds; instead, for the peak ratio method it is calculated via the error propagation formula dividing by the square-root of 2 the uncertainty of the velocity magnitude.

Table 1 Input and output quantities of the four uncertainty quantification methods

Method	Input quantities	Output quantities
Uncertainty surface (US)	PIV recordings Measured velocity field Processing algorithm	U_x^+: upper uncertainty bound of the *x*-velocity component U_x^-: lower uncertainty bound of the *x*-velocity component U_y^+: upper uncertainty bound of the *y*-velocity component U_y^-: lower uncertainty bound of the *y*-velocity component
Particle disparity (PD)	PIV recordings Measured velocity field Processing algorithm	U_x: uncertainty bound of the *x*-velocity component U_y: uncertainty bound of the *y*-velocity component
Peak ratio (PR)	Cross-correlation peak ratio	U: uncertainty bound of the velocity magnitude
Correlation statistics (CS)	Measured velocity field Image contributions to the cross-correlation function	U_x: uncertainty bound of the *x*-velocity component U_y: uncertainty bound of the *y*-velocity component

Uncertainty surface method

The uncertainty surface method (*US*) developed by Timmins *et al* (2012) uses the known response of a PIV algorithm to a number of error sources (the uncertainty surface) and the magnitudes of the error sources to determine the uncertainty of each vector. Since the uncertainty of a PIV calculation depends on the algorithm used (i.e. the software package along with all settings), the response of the algorithm to varying magnitude of each error source must be systematically tested to generate an *uncertainty surface* for that algorithm.

Synthetic images are used for this purpose. Once a surface has been generated, the uncertainty of each vector may be determined by measuring the value of each error source (particle image diameter, particle image density, particle displacement and shear, in work to date), and then querying the uncertainty surface based on those results.

Particle disparity method

In the particle disparity method (*PD*, Sciacchitano *et al*, 2013), the measured velocity field is used as a predictor to match the particle images of the recordings at the best of the processing algorithm (e.g. by image deformation or window shift). In each interrogation window, particle image pairs are sought for: in the ideal case (exact measurement), the particle images of the two recordings shall match perfectly; instead, in a real measurement the paired particle images do not match exactly and a positional disparity is present. The latter can be estimated with sub-pixel accuracy by particle image detection and a peak fitting algorithm. The measurement uncertainty is finally retrieved from the mean value and the statistical dispersion of the disparity vector within the interrogation window.

Peak ratio method

The peak ratio method (*PR*, Charonko and Vlachos, 2013) relies upon the assumption that, in the correlation plane, the error on the measured displacement is related to the cross-correlation peak ratio. The latter is defined as the ratio between the largest detectable peak (representing the particles displacement) and the second highest peak, which is linked to the combined effects of all error sources stemming from the image quality and the flow field. The uncertainty (U) of the measured displacement magnitude is retrieved from the peak ratio (PPR) by means of the empirical relationship (1):

$$U = 0.402\ PPR^{-0.84} \tag{1}$$

Correlation statistics method

Similar to the particle disparity method, the correlation statistics method (*CS*) proposed by Wieneke and Prevost (2014) quantifies the differences between the two interrogation windows mapped onto each other by the computed displacement field. However, instead of identifying the contribution of individual particles, this method analyses the overall contribution from all pixels to the shape of the correlation peak. The approach relies on the assumption that the PIV interrogation algorithm with predictor-correction scheme should always yield a symmetrical correlation peak when brought to convergence, i.e. with a final zero corrector displacement. However, the symmetrical correlation peak arises from the contributions not only of the particle images correctly matched, but also of the noise in the recordings. The correlation statistics method estimates the contribution of all pixels in the interrogation window to the asymmetry of the correlation peak, which on average leads to a symmetrical correlation peak. The standard deviation of the contributions provides an estimate of the expected asymmetry due to the image noise, which is related to the uncertainty of the displacement vector. In principle, this method takes all factors into account like remaining particle disparities, background image noise or out-of-plane particle motion affecting the correlation function.

From the description of the four methods, it emerges that the particle disparity and correlation statistics approaches rely upon the combined use of the PIV images, the cross-correlation signal and the measured velocity vector to determine the measurement uncertainty. The main difference between the two approaches is that the particle disparity method only accounts for the contribution of the detected particle image pairs, whereas the correlation statistics method includes the effect of all pixels in the interrogation window. Due to the intrinsic uncertainty in determining the position of individual particle images (Sciacchitano *et al*, 2013), the particle disparity method is expected to provide less accurate uncertainty estimates compared with the correlation statistics approach.

The peak ratio method quantifies the uncertainty from the ratio between highest and second highest peak of the correlation function. Such ratio is more traditionally regarded as an indicator of the reliability of the measurement, but it is indirectly related to the measured displacement, which is determined only by the position of the highest peak. The method is based on the empirical relation defined in equation (1) and requires input of calibration coefficients that are obtained with synthetic data.

Finally, the surface method is the only of the four approaches where the uncertainty quantification does not rely upon the analysis of the correlation function or of the image contributions to that. Monte Carlo simulations are conducted varying the magnitude of the chosen error sources. The uncertainty surface for the processing algorithm is thus built, which univocally associate a measurement uncertainty with a combination of error sources. The approach accounts for a limited number of error sources.

1.2 Uncertainty assessment by experiments

To evaluate the validity and accuracy of any uncertainty estimation method, the true measurement error should be known (Moffat, 1988). While the true error is readily available when conducting Monte Carlo simulations, it is typically unknown in real experiments and is usually difficult to access. For this reason, the experimental assessment of uncertainty quantification methods is recognized as a challenge.
In the present work, a dedicated series of experiments is conducted with two PIV systems in order to produce a very accurate estimate of the exact velocity field. The thorough description of the experiment is reported in Neal *et al* (2014). Here the rationale behind the simultaneous use of multiple PIV systems is briefly discussed. The *measurement system* records images in conditions representative of typical PIV experiments. At the same time, the second system, referred to as *high dynamic range (HDR) system*, records images at higher digital resolution (typically by factor 3 to 4) and with optimized imaging conditions (particle image size of two pixels). As a result, the HDR system delivers measurements at significantly higher dynamic velocity range (Adrian, 1997). The idea behind the use of two systems is that, for a given velocity, the HDR system measures a displacement discretized over a larger number of pixels than the measurement system: hence, even if the two systems may have comparable absolute uncertainty, the relative uncertainty of the HDR system (defined as the ratio between absolute uncertainty and measured displacement) is three to fourfold lower than that of the measurement system.
A concurrent, independent hot-wire measurement is compared to the HDR results to further verify that the HDR measurements may be treated as reference, as discussed by Neal *et al* (2014).
Due to the lower relative uncertainty, for the purposes of the present work, the HDR system measurements are regarded as the reference velocity field and used to estimate the actual error, which is employed to validate the different PIV uncertainty quantification methods. Note that, although it is common practice to evaluate the uncertainty at 95% confidence level (Coleman and Steele, 2009), in the present work 68% confidence level is used for a more accurate assessment of the uncertainty quantification methods via the uncertainty coverage analysis, which will be discussed in section 3.

2 Setup of the experiments

The experiments were conducted at the Experimental Fluid Dynamics Laboratory of Utah State University using a jet facility with rectangular nozzle of aspect ratio 7.2 (width 72.8 mm, height 10.2 mm). The facility is the same as that used in the experiments reported by Wilson and Smith (2013). The jet exit velocity was set to 5 m/s, yielding a Reynolds number based on the nozzle height of $Re_h = 3{,}000$. Recordings were acquired in continuous mode at sampling rate of 5,000 and 10,000 Hz. One camera normal to the measurement plane was used for the measurement system (LaVision HighSpeedStar 5, CMOS, 12 bit, 1,024×1,024 pixels, 17 μm pixel pitch, 3,000 frames per second at full resolution). The PIV HDR system was composed by two cameras in stereoscopic configuration (LaVision HighSpeedStar 6, CMOS, 12 bit, 1,024×1,024 pixels, 20 μm pixel pitch, 5,400 frames per second at full resolution). For a thorough description of the setup of the experiment, the reader is referred to Neal *et al* (2014). The configuration of the experiment is illustrated in figure 1.
The recordings were processed with the LaVision DaVis 8.1.6 software. For the measurement system, the final interrogation window size was 16×16 pixels and an overlap factor of 75% was selected; for the HDR system, final

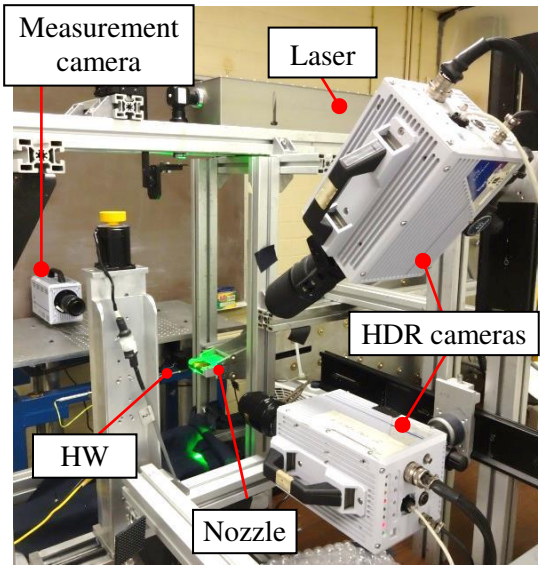

Figure 1 Setup of the experiment

windows of 32×32 pixels size with 75% overlap were employed.
Measurements were conducted in several flow regions that exhibit flow features typically encountered in PIV experiments. These regions included the potential core ($x/h \leq 1$, where x indicates the streamwise direction), the unsteady inviscid jet core ($x/h \approx 3 \div 4$) and developed turbulent region ($x/h \approx 19$). Moreover, different imaging conditions were taken into account in terms of particle image diameter and seeding density. Also the effect of out-of-plane motion was investigated by tilting the laser sheet with respect to the streamwise direction by16 degrees.

3 Results

3.1 Unsteady inviscid jet core region

In this section, the comparative assessment of uncertainty quantification methods is conducted in the unsteady jet core region where vortices are formed periodically due to the growth of Kelvin-Helmholtz instabilities ($x/h \approx$ 3-4; Neal *et al*, 2014).
The cross-stream profiles of the time-averaged velocity magnitude and normal stress are displayed in figure 2. The time-averaged profile is flat in the jet core and features a shear layer resulting in a shear rate of the images of approximately 0.15 px/px at the locations $y/h = \pm 0.5$. The normal stress profile shows the presence of large amplitude fluctuations within the shear layer, due to the formation and growth of Kelvin-Helmholtz vortices. Fluctuations of the order of 10% of the centreline time-averaged axial velocity are found within the jet core, which are associated with the accelerations induced by the Kelvin-Helmholtz vortices. The best estimate of the actual error, computed as the difference between measured velocity and HDR velocity, exhibits a normal distribution centred about zero (figure 3). The contribution of random errors is more than one order of magnitude larger than that of systematic errors (mean bias error: $\mu = -0.005$ px; standard deviation of the actual error: $\sigma = 0.056$ px).

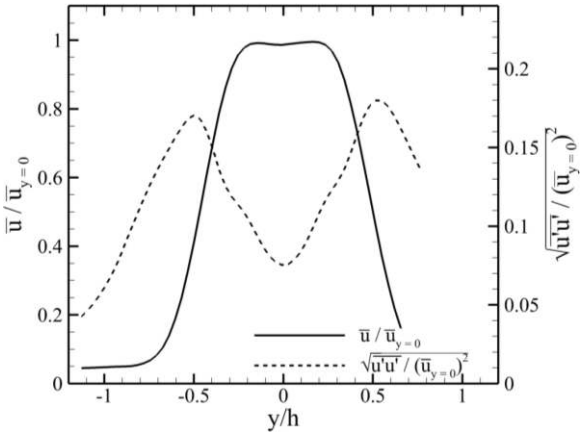

Figure 2 Cross-stream profile of the time-average velocity magnitude (continuous line) and of the normal stress (dashed line)

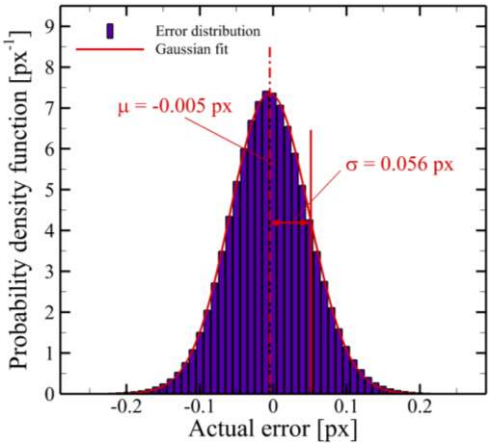

Figure 3 Probability density function of the actual error

Figure 4 shows an instantaneous cross-stream profile of the stream-wise velocity as computed with the measurement and the HDR-PIV system. The uncertainty bands at 68% confidence level are evaluated with the four uncertainty quantification methods. The measured profile is consistent with the HDR profile, with differences up to 0.1 pixels in the jet core ($y/h \sim 0$) and in the shear layer ($y/h \sim \pm 0.5$). Note that the HDR profile is defined only in $y/h = [-1.1, 0.8]$ due to the smaller size of the HDR measurement domain. The results show that for all the methods, the magnitude of the uncertainty bands is comparable with the actual error magnitude. However, the peak ratio method appears to overestimate the uncertainty; in fact, the HDR profile falls within the uncertainty bands for most of the measurements, while this was expected to occur only for 68% of the measurements. The root-mean-square profiles of figure 5 confirm that, in the present case, the peak ratio overestimates the uncertainty by about factor 2. The particle disparity method also overestimates the measurement uncertainty, but to a lesser extent (approximately 30%). Instead, the uncertainty estimated with the correlation statistics and uncertainty surface approaches follow more closely the actual error value.

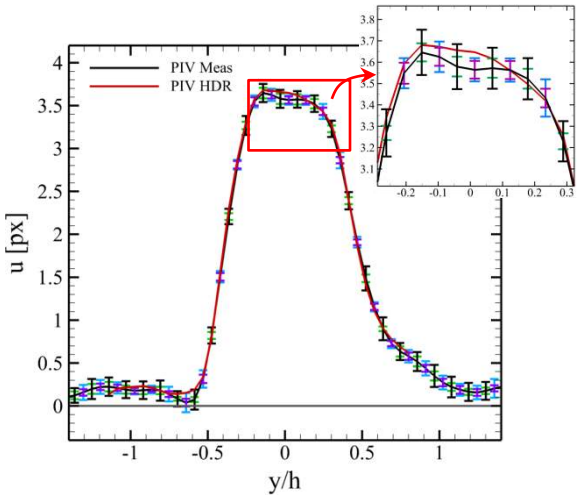

Figure 4 Instantaneous cross-stream profile obtained with the measurement system (black line) and with the HDR system (red line) with uncertainty bands at 68% confidence level: green: surface method; light blue: particle disparity method; black: peak ratio method; purple: correlation statistics method

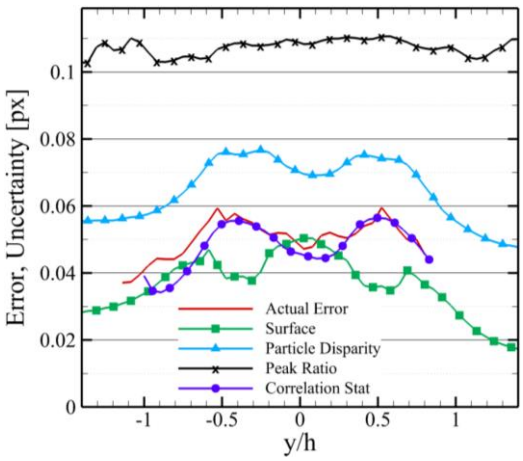

Figure 5 Comparison between actual error standard deviation and estimated uncertainty root-mean-square at $x/h = 2.9$

A more representative way to evaluate the reliability of the estimated uncertainty consists in computing the *uncertainty coverage*, which is defined as the percentage of measurements for which the exact value is contained within the uncertainty bands (Timmins *et al*, 2012). By definition, the uncertainty coverage should equal the confidence level (Coleman and Steele, 2009), that in this case is 68%; therefore, the closer the uncertainty coverage to 68%, the more accurate the uncertainty estimation. The results reported in table 2 confirm that the peak ratio method overestimates the uncertainty; in fact, for more than 90% of the measurements the true value is found within the uncertainty bounds. Also the coverage obtained with the particle disparity method slightly exceeds the expected value. Instead, uncertainty surface and correlation statistics methods slightly underestimate the uncertainty, yielding a coverage between 50% and 60%.

Table 2 Minimum and maximum estimated uncertainties and uncertainty coverage for the four methods: uncertainty surface (US), particle disparity (PD), peak ratio (PR) and correlation statistics (CS). The root-mean-square of the actual error is 0.056 pixels. The uncertainty has been estimated at 68% confidence level, thus the uncertainty coverage should ideally be equal to 68%

	US	PD	PR	CS
Min estimated uncertainty [px]	0.012	0.012	0.030	0.000
Max estimated uncertainty [px]	0.152	0.442	0.281	0.500
RMS estimated uncertainty [px]	0.041	0.073	0.108	0.049
Uncertainty coverage	52%	76%	94%	58%

The velocity time series is extracted from a point of the jet core to investigate the instantaneous measurement error (figure 6-a). Whereas the actual velocity is characterized only by low frequency fluctuations (below 100 Hz) ascribed to the acceleration induced by the Kelvin-Helmholtz vortices, the measurement system returns a velocity time history affected by high frequency fluctuations due to random noise. In figure 6-b, the actual error time series is computed as the difference between HDR and measurement velocity: the error is dominated by the random component with peaks exceeding 0.1 px, and it follows a Gaussian distribution (figure 6-c; skewness: –0.080; excess kurtosis: 0.028). Ideally, the standard uncertainty, which for Gaussian error distribution corresponds to the expanded uncertainty at 68% confidence level, should yield a constant value equal to the standard deviation of the error distribution (Coleman and Steele, 2009). The time series of figure 7 show that the uncertainty evaluated with the four methods is approximately constant in time, but exhibits random fluctuations due to the finite information employed in the uncertainty quantification. In fact,

according to Ahn and Fessler (2003), the expected spread of uncertainty is proportional to $1/\sqrt{[2(N-1)]}$, being N the number of particle image pairs contained in the interrogation window, which in the present test case is about 11. Hence, the uncertainty is expected to exhibit random fluctuations of the order of 20% of the mean estimated value.

The results also show that the uncertainty root-mean-square (rms) agrees with the actual error rms within 0.005 px when using the surface or correlation statistics methods; in contrast, peak ratio and particle disparity methods yield an uncertainty rms that overestimates the actual error by above 0.02 px.

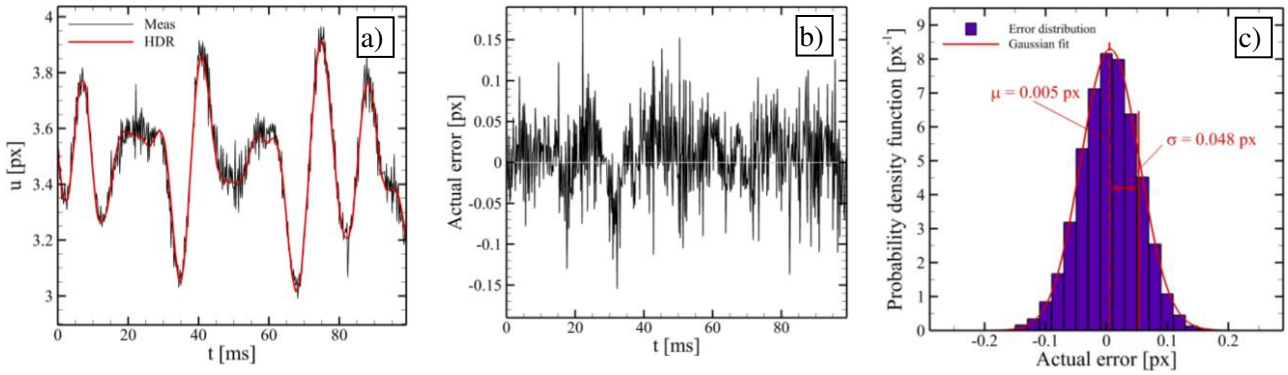

Figure 6 (a) Velocity time series at x/h = 2.9 and y/h =0 obtained with the measurement and the HDR system. (b) Actual error time series. (c) Actual error distribution

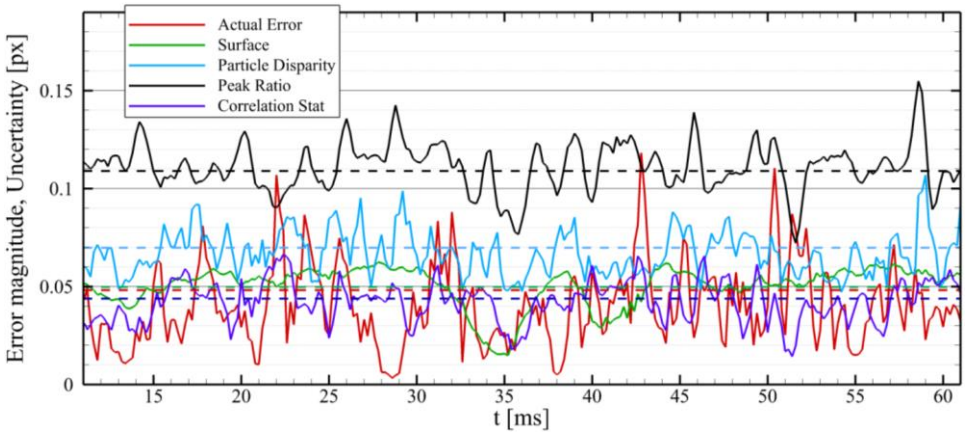

Figure 7 Actual error magnitude and uncertainty evaluated from the four methods at point x/h = 2.9, y/h =0. The root-mean-square of each series is displayed as a dashed curve

3.2 Effect of out-of-plane motion

The effect of the out-of-plane motion is investigated in the potential core region. The laser sheet is tilted by 16 degrees with respect to the jet exit direction so that a non-null component in the direction normal to the laser sheet is realized (indicated with z in figure 8; see Neal *et al*, 2014, for more details on the setup of the experiment). In the present case, the laser sheet thickness is Δz = 1.7 mm (about 12 px of the measurement system).

Figure 9 reports the time-averaged x- and the z-velocity components (being z the out-of-plane direction) measured by the HDR system and expressed in pixel units of the measurement system. As expected, the largest out-of-plane displacement occurs in the jet core, where also the axial velocity is the highest; the maximum out-of-plane displacement between subsequent recordings is approximately 18% of the laser sheet thickness. Outside the jet the fluid is approximately at rest.

The measurement error is strongly affected by the out-of-plane displacement. The error distribution of figure 10 shows how the out-of-plane motion yields a major increase of the random error component, with the actual error standard deviation increasing by factor 5 (from 0.04 px to 0.23 px). It is also noticed that the two distributions are centred about zero, but exhibit opposite mean bias errors (–0.07 px in the jet core, 0.06 px in the stagnant region). Although perspective errors may be the cause of this behaviour (the optical axis of the

measurement camera might be not exactly normal to the laser sheet), a conclusive explanation has not been found yet.

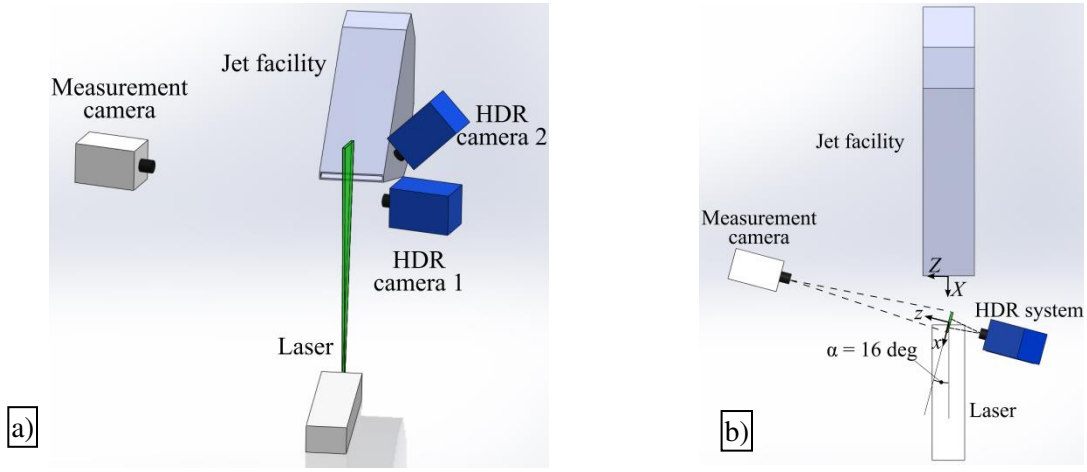

Figure 8 Schematic representation of the experimental setup. (a) Three-dimensional view; (b) top view. The laser sheet is tilted by 16 degrees with respect to the jet axis direction. The jet axes system is indicated with (*X*, *Y*, *Z*), the measurement axes system with (*x*, *y*, *z*). In the actual experiment, the flow was illuminated from above the jet facility

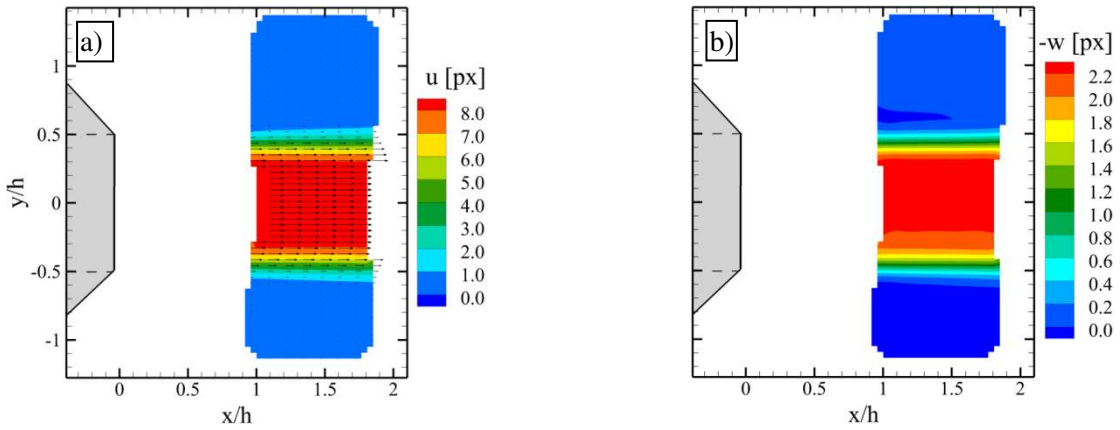

Figure 9 Time-averaged *x*-velocity component (a) and *z*-velocity component (b) measured by the HDR system. Both components are expressed in pixel units of the measurement system

The comparison between estimated uncertainty and actual error is reported in figure 11. The actual error distribution of figure 11-e clearly shows that the largest error occur in the jet core, where the out-of-plane displacement is the highest, while errors below 0.05 px take place in the outer region. The uncertainty estimation obtained from particle disparity and correlation statistics methods is more consistent with the actual error distribution (figure 11-b and -d): the estimated uncertainty exceeds 0.2 pixels in the jet core and drops below 0.1 px in the stagnant region, where the out-of-plane displacement (as well as the in-plane displacement) is negligible. Here, the particle disparity method yields overestimated uncertainty values due to the intrinsic inaccuracy in determining the particle image disparity (see figure 11-f). The uncertainty evaluated with the peak ratio method exhibits lower sensitivity to the actual error value (figure 11-c): as can be seen also from the uncertainty profile extracted of

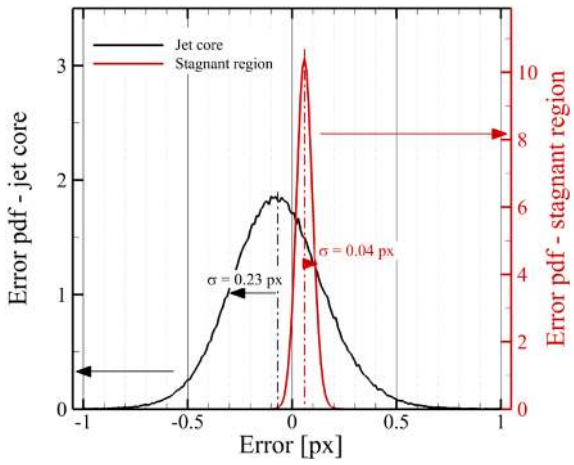

Figure 10 Actual error distribution in the jet core and in the stagnant region

figure 11-f, the estimated uncertainty is approximately uniform along the *y*-direction and only minor differences of the order of 0.06 px are retrieved between jet core and outer region. Finally, the surface method strongly underestimates the uncertainty, especially in the jet core (figure 11-a); the latter result was anticipated, because the approach does not account for errors stemming from out-of-plane motion.

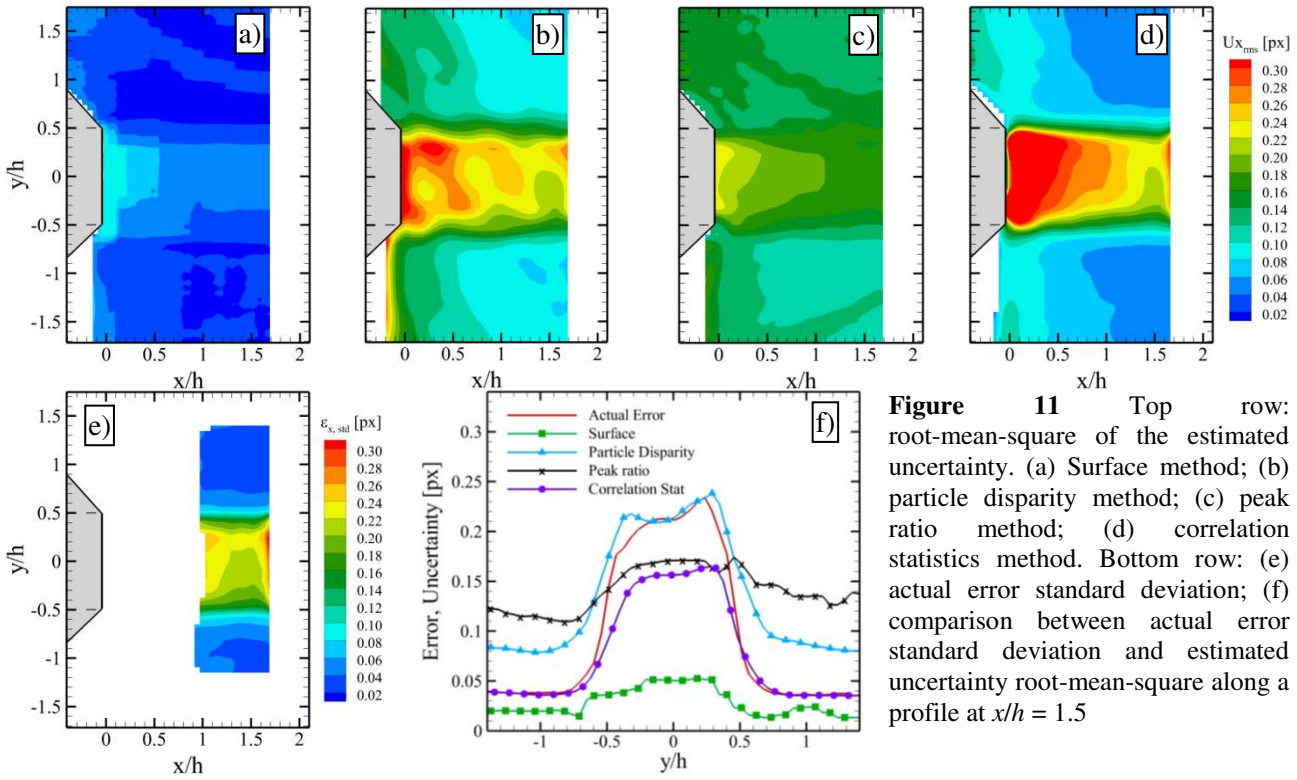

Figure 11 Top row: root-mean-square of the estimated uncertainty. (a) Surface method; (b) particle disparity method; (c) peak ratio method; (d) correlation statistics method. Bottom row: (e) actual error standard deviation; (f) comparison between actual error standard deviation and estimated uncertainty root-mean-square along a profile at $x/h = 1.5$

The uncertainty statistics and coverage in the jet core are reported in table 3. The results confirm that both particle disparity and correlation statistics methods consistently estimate the uncertainty, yielding a coverage that approaches the theoretical value (68%). It is also confirmed that the peak ratio method slightly underestimates the uncertainty in this region, while for the surface method the underestimation is major.

Table 3 Uncertainty statistics and coverage in the jet core. Uncertainty surface (US), particle disparity (PD), peak ratio (PR) and correlation statistics (CS) methods. The root-mean-square of the actual error in this region is 0.237 pixels. The uncertainty has been estimated at 68% confidence level, thus the uncertainty coverage should ideally be equal to 68%

	US	PD	PR	CS
Min estimated uncertainty [px]	0.012	0.054	0.053	0.030
Max estimated uncertainty [px]	0.160	0.783	0.284	0.707
RMS estimated uncertainty [px]	0.052	0.229	0.172	0.233
Uncertainty coverage	19%	64%	53%	65%

3.3 Effect of small particle images

A test case with poorly sampled particle images (diameter of 1 pixel) is selected to examine how the different uncertainty quantification algorithms cope with peak-locking errors. The seeding density is approximately 0.05 particles per pixel (ppp) for the measurement system. The potential core region is considered in this case. Due to the small particle image diameter in the measurement system recordings, peak locking errors occur that bias the estimated displacement towards integer values, as illustrated in figure 12.

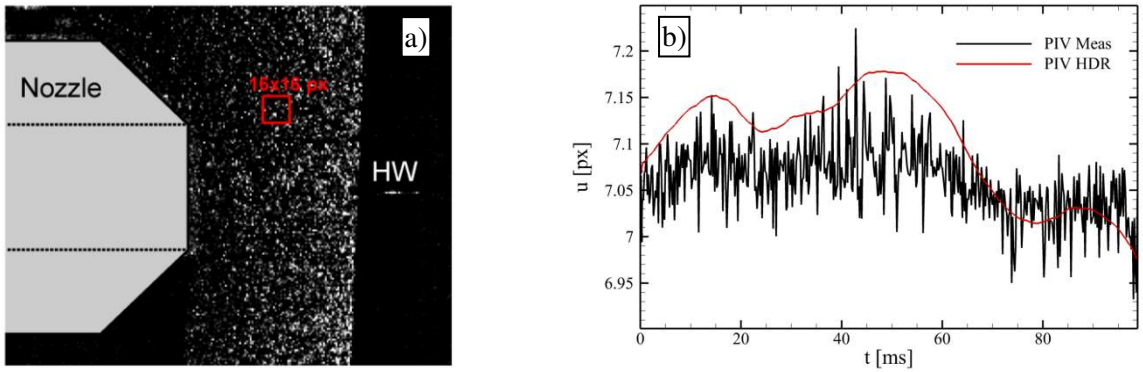

Figure 12 (a) Raw image. The nozzle and the hot-wire probe (HW) are indicated on the image. Note that the particle images have diameter of approximately 1 pixel. (b) Fragment of the velocity time history in the potential core: in the measurement system, actual displacements between 7.1 and 7.2 pixels are typically biased towards 7 pixels due to peak locking errors

The actual error is approximately 0.08 px in the jet core, whereas it rises up to 0.15 px in the shear layer (see figures 13-e and -f). The uncertainty contours of figures 13-a to -d show that the four methods consistently evaluate higher uncertainty in the shear layer. Nevertheless, the surface method provides values underestimated by a factor 2 both in the jet core and in the shear layer (figure 13-a). We note that the particle image diameter found with the method of Warner and Smith (2014), which is used in the US method, returned a particle image diameter of 1.7 pixels. The difference in this method and the method of Adrian and Westerweel (2011) (which results in a particle image diameter of 1.4) is only pre-processing of the image to remove background noise. Modifying the particle image size to 1.4 results in a doubling of the uncertainty from the US method, which shows that the uncertainty estimation is extremely sensitive to particle image size near 1.4 pixels.
Correlation statistics and particle disparity approaches yield an uncertainty distribution that is consistent with the actual error (see figures 13-b and -d). Instead, the uncertainty estimated with the peak ratio method exhibits lower variations (about 0.06 px) among the different regions of the flow field (core, shear layer and stagnant flow), as illustrated in figure 13-c.

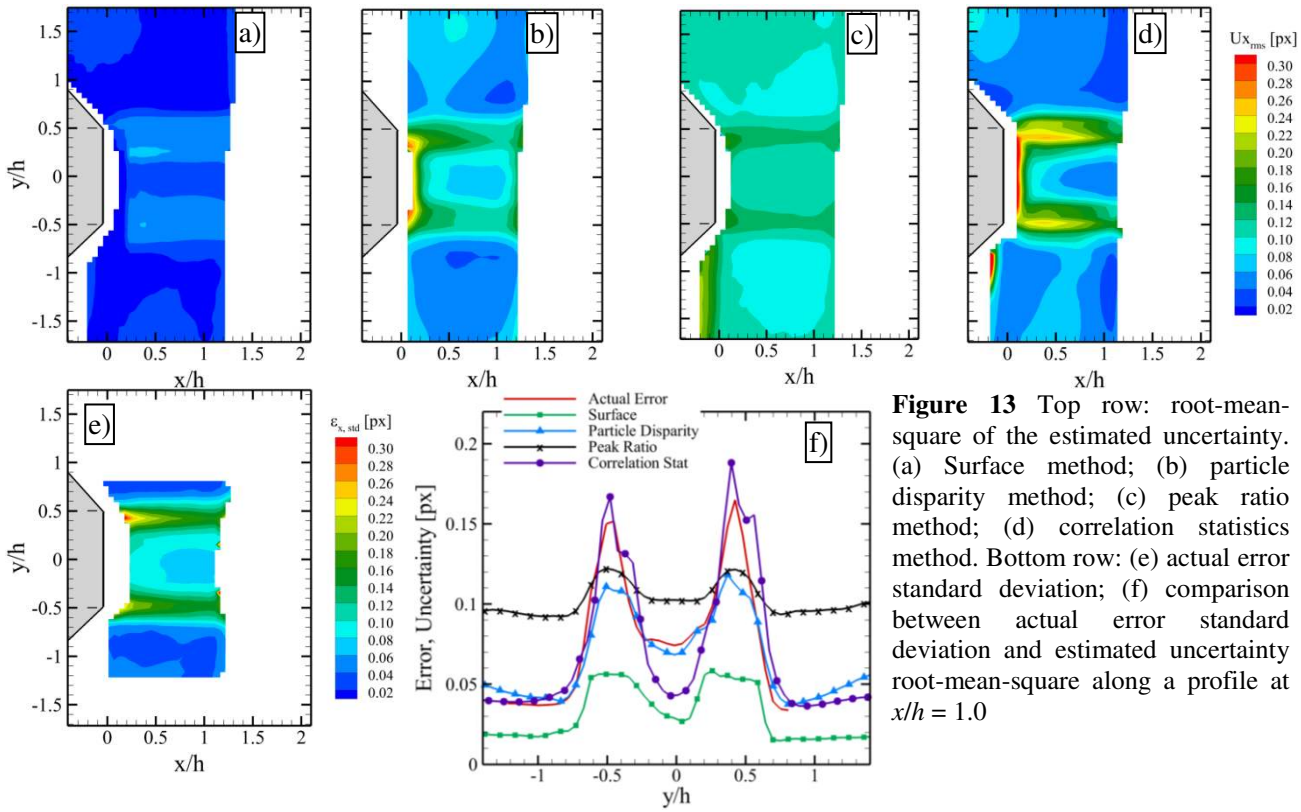

Figure 13 Top row: root-mean-square of the estimated uncertainty. (a) Surface method; (b) particle disparity method; (c) peak ratio method; (d) correlation statistics method. Bottom row: (e) actual error standard deviation; (f) comparison between actual error standard deviation and estimated uncertainty root-mean-square along a profile at $x/h = 1.0$

The error distribution at a point of the potential core (x/h = 1, y/h = 0) is shown in figure 14. Such distribution is not Gaussian: the highest peak at ε = 0 px does not correspond to the mean error (μ = –0.033 px). Both skewness and excess kurtosis, which are much larger with respect to those evaluated in section 3.1 (–0.191 and 0.153, respectively), confirm that the error distribution is not normal. The latter finding suggests that the errors at that point stem from multiple parent populations. This can be explained by the presence of peak locking: when the actual fractional displacement is null, peak locking errors are negligible and the error parent population is expected to be narrow and centred around zero; instead, for fractional displacements of 0.1-0.2 px, larger peak locking errors are expected (Raffel *et al*, 2007), resulting in a wider error parent population not centred around zero.
The time series of the error magnitude is extracted from the point x/h = 1, y/h = 0 and compared with the estimated uncertainty (see figure 15). Contrary to the error time series shown in figure 7, where a constant error in time with only random fluctuations is found, the present result yields a systematic error component, which is not constant it time, but varies between less than 0.01 px (see for instance 550 ms ≤ t ≤ 600 ms and t ≅ 950 ms) and 0.1 px (e.g. 400 ms ≤ t ≤ 450 ms and 800 ms ≤ t ≤ 900 ms). The highest systematic errors occur when the actual displacement is about 7.3 px (figure 16). This, along with the small particle image diameter, suggests that the systematic error is mainly caused by peak locking (Westerweel, 1997).
The uncertainty estimated with the four methods is also displayed in figure 15 for comparison. Even though different uncertainty values are obtained (e.g. the peak ratio method returns an uncertainty time-series approximately constant about 0.1 px, whereas the surface approach yields a minimum uncertainty estimate below 0.02 px), all the time series exhibit a correlation with the actual error magnitude. Higher uncertainty is estimated at the locations where the error magnitude is the highest (e.g. at time instants about t = 400 ms and 800 ms), whereas low error magnitudes are associated with uncertainty values typically below 0.05 px, except for the peak ratio method.

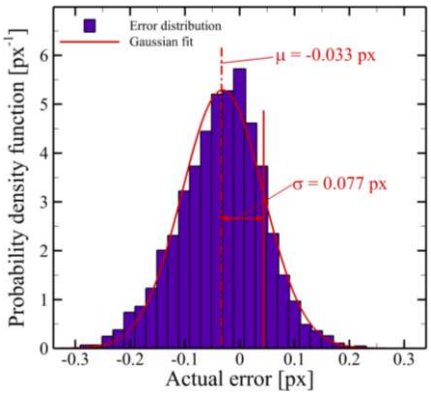

Figure 14 Actual error distribution at x/h =1, y/h=0

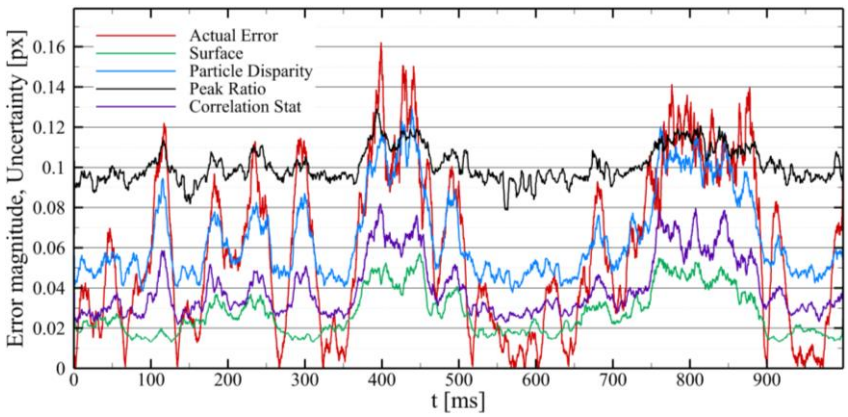

Figure 15 Actual error magnitude and uncertainty time histories at x/h =1, y/h=0. All the time series have been filtered with a moving average top-hat filter on a kernel of 6 ms to attenuate random fluctuations

The normalized cross-correlation function between actual error magnitude and estimated uncertainty has been computed to assess the dependence between the two quantities. The normalised cross-correlation attains a unit value when the two variables are identical or linearly dependent, while it drops to 0 when they are linearly independent (De Groot, 1989). The results of figure 17 show that all the four methods yield maximum cross-correlation values exceeding 0.70, meaning that the estimated uncertainty is strongly correlated with the actual error magnitude. The highest correlation is achieved with the particle disparity method, which returns a value exceeding 0.90.

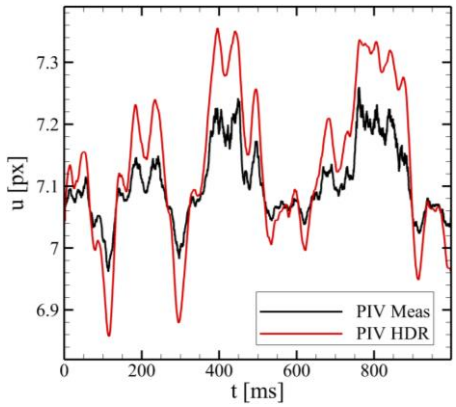

Figure 16 Velocity time history at at x/h =1, y/h=0 as measured by the HDR and the measurement systems. The time series have been filtered with a moving average top-hat filter on a kernel of 6 ms to attenuate random fluctuations

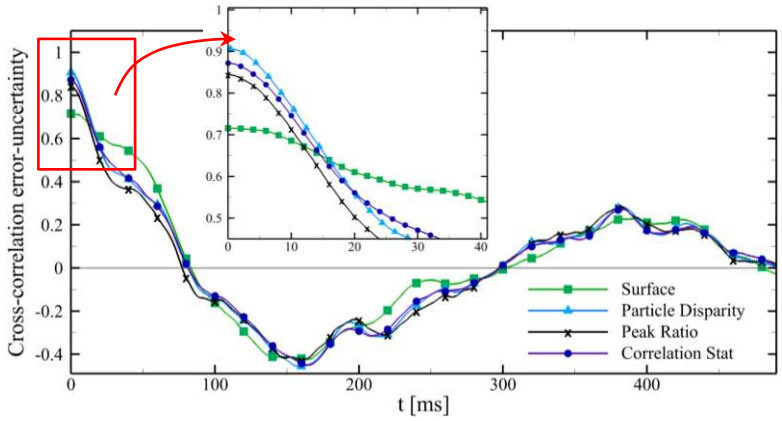

Figure 17 Cross-correlation function between actual error magnitude and uncertainty time series

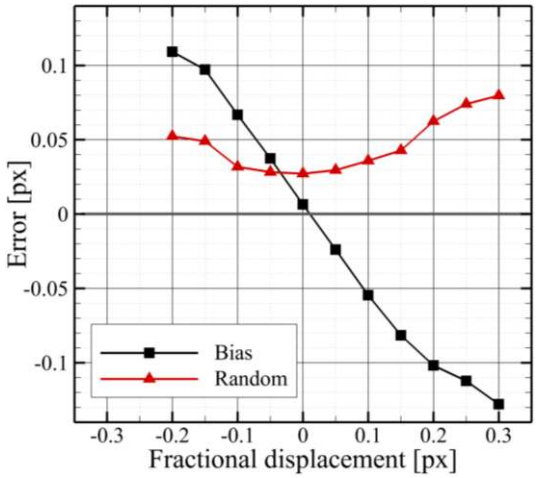

Figure 18 Mean-bias and random error components as a function of the fractional displacement at x/h = 1, y/h = 0

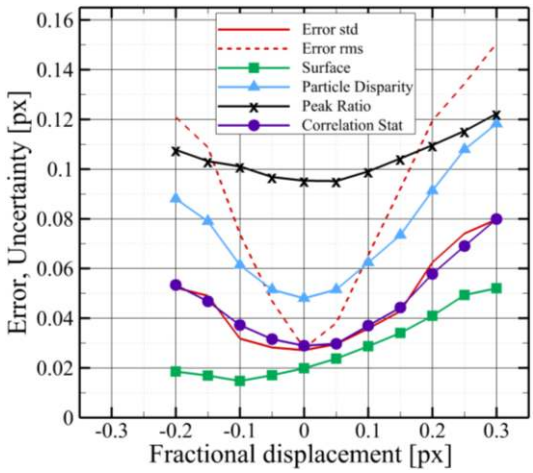

Figure 19 Error and uncertainty as a function of the fractional displacement at x/h = 1, y/h = 0

The systematic and random error components are extracted from the error time series of figure 15 to assess how the four methods are able to estimate the uncertainty stemming from those. Figure 18 puts in evidence that severe peak locking errors occur: the mean bias error is the minimum for zero fractional displacement and raises up to above 0.1 px for fractional displacements exceeding 0.2 px. Also the random error component is the minimum at zero fractional displacement, which is consistent with the numerical simulations of Scarano and Riethmuller (2000).

Both random and systematic errors increase with the fractional displacement. As a result, regions of fractional displacement close to zero are characterized by both low mean bias error (below 0.01 px) and low random error (below 0.03 px); here, also the uncertainty is expected to be low, because by definition it is an estimate of the standard deviation of the parent population from which the error stems. Instead, for fractional displacements exceeding 0.15 px both systematic and random errors are significantly larger; hence, also the uncertainty is expected to rise. This explains the correlation between uncertainty and error magnitude shown in figures 15 and 17.

It is important to remark here that in more conventional PIV experiments where the error is dominated by the random component, the uncertainty is typically uncorrelated from the error magnitude, as it has been shown in section 3.1. Instead, the presence of systematic errors comparable to or larger than random errors may lead to correlation between error magnitude and uncertainty.

The comparison between actual error and estimated uncertainty as a function of the fractional displacement is shown in figure 19. The results show that US and CS methods estimate only the random component of the

error; in particular, the CS-uncertainty exhibits excellent agreement with the actual error standard deviation. The PD approach partly detects also the bias error component and estimates larger uncertainty (up to 0.12 px) for fractional displacement of 0.3 pixels. Finally, the PR method shows a higher "floor" for fractional displacement close to zero, meaning that for sub-pixel displacements between -0.1 and 0.1 px the uncertainty due to both random and bias error components is largely overestimated.

3.4 Effect of low seeding density

The same test case of section 3.3 is replicated with lower seeding density (approximately 0.02 ppp, see figure 20) to investigate the response of the four methods to such error source. In this case, each interrogation window of size 16×16 pixels contains on average approximately 5 particle images. Consequently, the accuracy of those methods that quantify the uncertainty from a statistical analysis of the particles contribution to the correlation peak is expected to decrease, due to the reduced information contained in each window.

Figure 21 shows the comparison between actual error and estimated uncertainty along a profile at $x/h = 1$. With respect to the case presented in figure 13, higher error up to 0.25 pixels is obtained in the shear layer. The peak ratio method yields an estimated uncertainty profile that resembles that for the larger seeding density case: the uncertainty is approximately uniform about 0.1 px and slightly larger values (0.13 px) are achieved in the shear layer. Also the particle disparity approach provides an uncertainty estimate that does not differ significantly from that of the previous test case. The method underestimates the uncertainty in the shear layer; as anticipated, this is attributed to the reduced number of particle images contained in the interrogation window, which precludes the convergence of the statistical analysis from which the uncertainty is evaluated. For the correlation statistics method, the underestimation is lower and uncertainty peaks up to 0.2 pixels are estimated at the shear layer locations. Finally, the surface method yields uncertainty values that better approximate the error peaks.

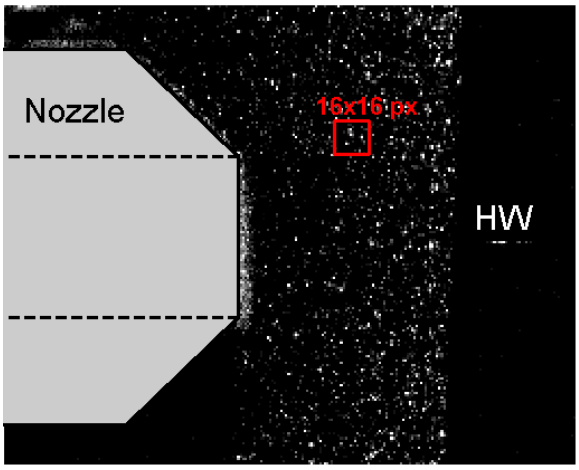

Figure 20 Raw image for the test case of seeding density of approximately 0.02 ppp

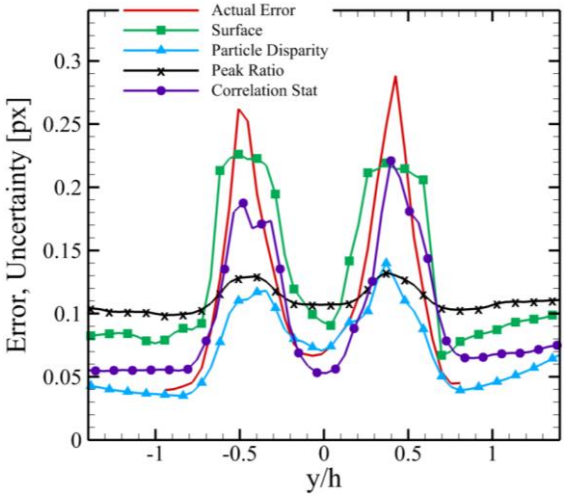

Figure 21 Comparison between actual error standard deviation and estimated uncertainty root-mean-square along a profile at $x/h = 1.0$

The uncertainty statistics and coverage reported in table 4 confirm that for the present case the surface method provides a more reliable uncertainty estimate than those methods that rely upon the analysis of the image contributions to the correlation. This is ascribed to the fact that the surface method makes use of numerical simulations that reproduce the experimental conditions; therefore, its performance does not degrade for low seeding density.

Table 4 Uncertainty statistics and coverage. Uncertainty surface (US), particle disparity (PD), peak ratio (PR) and correlation statistics (CS) methods. The root-mean-square of the actual error in this region is 0.258 pixels. The uncertainty has been estimated at 68% confidence level, thus the uncertainty coverage should ideally be equal to 68%

	US	PD	PR	CS
Min estimated uncertainty [px]	0.012	0.008	0.006	0.006
Max estimated uncertainty [px]	0.416	1.156	0.284	1.286
RMS estimated uncertainty [px]	0.189	0.106	0.117	0.155
Uncertainty coverage	60%	38%	51%	47%

4 Conclusions

The present work has discussed a comparative assessment of four uncertainty quantification methods for PIV data, namely the uncertainty surface approach (Timmins *et al*, 2012), the particle disparity method (Sciacchitano *et al*, 2013), the peak ratio method (Charonko and Vlachos, 2013) and the correlation statistics approach (Wieneke and Prevost, 2014). A dedicated experimental data base has been generated to enable the assessment; details of the experiment are reported in Neal *et al* (2014). The peculiarity of the data base is that the reference instantaneous velocity field is known via a more accurate measurement conducted by an auxiliary PIV system, defined the HDR (high dynamic range) system. The measurement error is computed as the difference between measured and HDR velocity and therefore is estimated with high accuracy. This quantity is used to evaluate the reliability of the uncertainty estimate.
The data base has been used to investigate the capability of the four uncertainty quantification methods to estimate the instantaneous local uncertainty in presence of error sources typically encountered in PIV experiments. Strengths and weaknesses of the existing uncertainty quantification approaches have been put in evidence.

It has been shown that the approaches that quantify the uncertainty from the image contributions to the shape of the correlation peak (namely particle disparity and correlation statistics methods) exhibit satisfactory sensitivity to the actual measurement error: higher uncertainty is typically estimated in regions of larger error. In the presented test cases, uncertainty peaks up to 3-4 times the minimum estimated value have been retrieved consistently with the actual error trend. The sensitivity of those methods is ascribed to the fact that the uncertainty is estimated from the shape of the correlation peak, which affects directly the measured displacement. This work has also revealed that the particle disparity method typically overestimates the uncertainty associated with error values below 0.04 pixels: such behaviour has been anticipated and is due to the intrinsic uncertainty of the approach in determining the position of individual particle images, as discussed in Sciacchitano *et al* (2013).
The peak ratio method exhibits lower sensitivity to variations of the actual error: in the presented cases, the estimated uncertainty typically varies by about 50% between regions of highest and lowest error, even if the error variation exceeds factor 5. The lower sensitivity with respect to e.g. correlation statistics and particle disparity approaches can be explained by the fact that the method quantifies the uncertainty from a quantity, namely the cross-correlation peak ratio, which is not directly related to the measured displacement.
The surface method does not make use of information stemming from the cross-correlation function or the image contributions to that, but instead employs Monte Carlo simulations that reproduce the experimental conditions. The approach is particularly valuable for low seeding density, when little information is contained in the PIV recordings and image-based methods (particle disparity and correlation statistics) may yield results where the statistical convergence is not reached. The main limitation is that not all the error sources are accounted for: in the current implementation, the method is insensitive to errors arising from out-of-plane motion, which constitute a relevant component in turbulent flow investigation.
The lessons learned in the present investigation are expected to promote further advances in the direction of developing of a consolidated methodology for the *a-posteriori* uncertainty quantification of PIV data.

References

Adrian RJ (1997), Dynamic ranges of velocity and spatial resolution of particle image velocimetry, Meas Sci Technol **8** 1393

Adrian RJ and Westerweel J (2011), Particle Image Velocimetry, Cambridge University Press

Ahn S and Fessler JA (2003), Standard errors of mean, variance, and standard deviation estimators, http://web.eecs.umich.edu/~fessler/papers/files/tr/stderr.pdf

Charonko JJ and Vlachos PP (2013), Estimation of uncertainty bounds for individual particle image velocimetry measurements from cross correlation peak-ratio, Meas Sci Technol **24** 065301 (16pp)

Coleman HW and Steele WG (2009), Experimentation, Validation, and Uncertainty Analysis for Engineers, 3rd edn (Hoboken, NJ: Wiley) doi:10.1002/9780470485682

Lecordier B, Demare D, Vervisch LMJ, Réveillon J and Trinité M (2001), Estimation of the accuracy of PIV treatments for turbulent flow studies by direct numerical simulation of multi-phase flow, Meas Sci Technol **12** 1382

Moffat RJ (1988), Describing the uncertainties in experimental results, Exp Therm Fluids Sci **1**:3-17

Neal DR, Sciacchitano A, Smith BL and Scarano F (2014), Collaborative framework for PIV uncertainty quantification: the experimental database, 17th International Symposium on Applications of Laser Techniques to Fluid Mechanics, Lisbon, Portugal

Raffel M, Willert CE and Kompenhans J (2007), Particle image velocimetry – A practical guide, Springer, New York

Scarano F and Riethmuller ML (2000), Advances in iterative multigrid PIV image processing, Exp Fluids **29** pp. S51-S60

Sciacchitano A, Wieneke B and Scarano F (2013), PIV uncertainty quantification by image matching, Meas Sci Technol **24** 045302 (16pp)

Stanislas M, Okamoto J, Kähler CJ and Westerweel J (2005), Main results of the second international PIV challenge, Exp Fluids **39** 170-191

Timmins BH, Wilson BW, Smith BL and Vlachos PP (2012), A method for automatic estimation of instantaneous local uncertainty in particle image velocimetry measurements, Exp Fluids **53** pp. 1133-1147

Warner SO and Smith BL (2014), Autocorrelation-based estimate of particle image density for diffraction limited particle images, Meas Sci Technol **25** 065201 (10pp)

Wilson BM and Smith BL (2013), Uncertainty on PIV mean and fluctuating velocity due to bias and random errors, Meas Sci Technol **24** 035302 (15pp)

Wieneke B and Prevost R (2014), DIC uncertainty estimation from statistical analysis of correlation values, Conference Proceedings of the Society for Experimental Mechanics Series, pp 125-136

Westerweel J (1997), Fundamentals of digital particle image velocimetry, Meas Sci Technol **8** pp. 1379-1392